This article has been accepted for publication in IEEE Transactions on Power Electronics. This is the author's version which has not been fully edited and content may change prior to final publication. Citation information: DOI 10.1109/TPEL.2026.3724067

TPEL-Reg-2026-03-0006

Torque and Current Ripple Suppression in Integrated Chargers for Synchronous Reluctance Machines

G. Rizzoli, L. Vancini, *Member, IEEE*, M. Mengoni, *Member, IEEE,* L. Zarri, *Senior Member, IEEE*, A. Tani

***Abstract*—The automotive industry is increasing the voltage level of electric vehicles from 400 V to 800 V to reduce charging time without increasing the current levels. The vehicle wiring and the connectors that link the external DC fast charger to the internal battery impose limits on the maximum charging current for thermal, mechanical, and reliability reasons. Despite the advent of 800 V vehicles on the market, only a few charging stations support this higher voltage level. Consequently, electric vehicles must be designed to be compatible with 400 V DC charging stations, albeit with a slight increase in both the cost and weight of the powertrain components. The solution outlined in this study involves reconfiguring the electric motor and the inverter into a DC/DC boost converter to adapt the high-voltage battery to the voltage level of the off-board charger. During the charging process, several constraints should be considered for both the machine and off-board charger. These aspects include generating a zero-mean torque independently of the rotor position, minimizing the torque ripple, and minimizing the output-current ripple of the off-board charger. The analysis presented in this paper focuses on synchronous machines without permanent magnets.**

***Index Terms*—Integrated chargers, conductive charging, voltage-source interleaved converters, power electronics.**

I. INTRODUCTION

PRIVATE and commercial Battery Electric Vehicles (BEVs) intended for long distances in an extra-urban operations outside urban areas require a battery pack with large capacity, short recharging time, and recharging facilities distributed widely deployed across the road network [1]-[2]. Charging time shorter than 30 minutes can only be obtained using high-power off-board chargers (typically from 50 kW up to 350 kW), which are directly connected to the battery terminals bypassing the On-board Battery Charger (OBC) [3]-[4]. Technical standards SAE J1772 and IEC 61851 discipline the coordination between the vehicle and the off-board charger, including electrical safety requirements, connectors, communication protocols, and operating modes [5]. To achieve high-power levels, in 400 V BEVs, the charging current can easily reach 1 kA. Therefore, it is evident that electrical cables and charging connectors represent one of the most critical and highly stressed components of the system [6]-[7]. To avoid expensive, bulky, and critical connecting devices, the automotive industry is increasing the battery voltage from 400 V to 800 V to extend the charge power without increasing the current level, even though public infrastructure is not yet adequate to support 800 V vehicles [8]. However, a complete upgrade of the charging infrastructure does not seem feasible in the near future. Instead, a gradual transition period will be necessary, during which 400 V and 800 V charging stations will coexist. Consequently, 800 V vehicles must be equipped with a boost functionality to address the inherent incompatibility between 800 V batteries and 400 V chargers and to adapt to all the available charging stations. A standard solution involves using a dedicated on-board DC/DC boost converter to interface the battery to the off-board charger [9]. This approach is undoubtedly possible but requires an additional high-power density and low-cost converter, two features that are difficult to achieve simultaneously. Conversely, using the electric powertrain of the vehicle as a step-up DC/DC converter is a cost-effective way to solve the problem [10]. This approach has a minimal effect on the cost of the vehicle and provides a high level of integration [11]. The power rating of the traction inverter is similar to the one required for the high-power boost conversion, and the high-performance control unit of the traction inverter can easily implement these additional functionalities. However, the unconventional use of an electric machine as a coupled inductor requires careful electromagnetic analysis [12] and a dedicated control scheme. A fundamental requirement common to all the integrated charger configurations is that the vehicle must not move throughout the charging process. Although the machine is used as an inductor, the circulation of currents through the machine windings can spontaneously generate an electromagnetic torque [13]-[14]. If the torque cannot be suppressed during the charging process, it is recommended that a parking brake with an appropriate locking torque be installed. An alternative solution would be to decouple the machine shaft from the mechanical transmission using a clutch, which would increase the cost and complexity of the system.

Several machine-winding configurations have been proposed in the literature to use the traction machine as an inductor in integrated AC/DC and DC/DC battery chargers. Most previous studies focus on grid-connected AC/DC charging from single-phase or three-phase mains. In these systems, the main design objectives are typically the reduction of line-current distortion [15]-[17], Vehicle to Grid (V2G) functionality [18], the use of multiphase machines [19]-[20], the minimization of low-frequency torque ripple [21], and galvanic isolation capability [22]. Conversely, the problem considered in this paper is different: the traction drive is reconfigured as a DC/DC boost

The authors are with the Department of Electrical, Electronic and Information Engineering, University of Bologna, 40136 Bologna, Italy (e-mail: gabriele.rizzoli@unibo.it, luca.vancini4@unibo.it; michele.mengoni@ unibo.it; luca.zarri2@unibo.it; angelo.tani@unibo.it).

This work is licensed under a Creative Commons Attribution-NonCommercial-NoDerivatives 4.0 License.
For more information, see https://creativecommons.org/licenses/by-nc-nd/4.0/

This article has been accepted for publication in IEEE Transactions on Power Electronics. This is the author's version which has not been fully edited and content may change prior to final publication. Citation information: DOI 10.1109/TPEL.2026.3724067

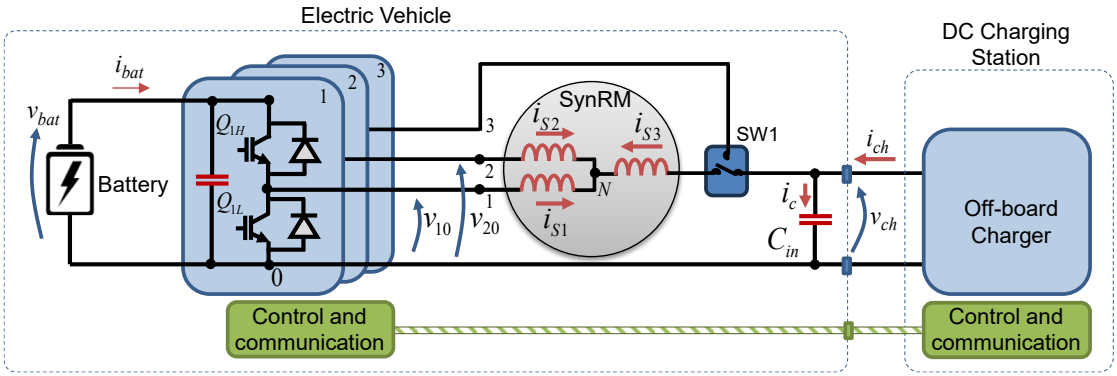

Fig. 1. Integrated boost charger to achieve compatibility between 800 V-battery vehicles and 400 V fast-charging stations.

converter to interface a 400 V off-board DC charger with an 800 V battery pack.

Only a limited number of works have addressed this DC/DC integrated charging scenario. In [23], the external DC charger is connected to the neutral point of the motor and the homopolar inductance of an IPM machine is used as the boost inductance. However, due to the low value of the homopolar inductance, an additional discrete inductor should be included in the circuit to limit the current ripple. To overcome this limitation, the integrated charger in [24] uses only two machine phases to exploit the larger differential inductances of the motor and improve energy efficiency. Although these works represent relevant contributions to DC integrated charging, a complete analysis of a synchronous reluctance machine used as the coupled inductor of a DC/DC boost charger, including zero-torque control, loss-oriented voltage selection, magnetic saturation, and the trade-off between charger-side current ripple and torque ripple, has not been fully addressed.

Among the possible machine-winding configurations, this paper analyzes the layout depicted in Fig. 1. The main advantage of this scheme is that it exploits the differential inductances of the machine and requires only a minimal reconfiguration of the electrical circuit when moving from the traction-drive configuration to the boost-charging configuration. In particular, only one machine phase must be disconnected from the inverter and connected to the off-board charger by means of the contactor SW1.

The proposed solution is specifically focused on synchronous machines without permanent magnets, such as Synchronous Reluctance Machines (SynRMs). This choice is attractive because the absence of permanent magnets avoids magnet-related torque contributions during charging, while the machine differential inductances can be used for the boost operation. At the same time, the anisotropic and nonlinear magnetic behavior of the SynRM requires a dedicated control strategy and a specific ripple analysis. In fact, the current references must be selected to regulate the charger-side voltage while ensuring zero average torque at any standstill rotor position. Moreover, the PWM carrier phase shift, rotor position, voltage ratio, charging current, and magnetic saturation affect both the current ripple injected toward the off-board charger and the residual torque ripple at the shaft.

Table I compares the proposed solution with closely related integrated charging approaches involving DC/DC boost operation, charging-torque analysis, or zero-torque operation. The aim of the comparison is not to rank the different solutions, since they address different machine configurations and charging scenarios, but to clarify the specific scope and contribution of the present work. The comparison shows that the novelty of this paper is not the general concept of reusing the traction drive for charging, but rather the modeling, control, and experimental validation of a SynRM-based DC/DC boost integrated charger for 400 V charger / high-voltage battery compatibility.

The main contributions of the paper are summarized as follows:

- A DC/DC boost integrated charging configuration based on a synchronous reluctance machine is analyzed for the compatibility between 400 V off-board DC chargers and higher-voltage battery packs.
- A current-reference generation strategy is derived to guarantee zero average torque at any standstill rotor position while regulating the charger-side voltage.
- A loss-oriented criterion for selecting the charger-side voltage reference is introduced and supported by numerical loss simulations including machine Joule losses and inverter conduction and switching losses.
- The effect of rotor position, magnetic saturation, charging current, voltage ratio, and PWM carrier phase shift on the charger-side current ripple and residual torque ripple is analyzed.
- The theoretical analysis is experimentally validated on a reduced-scale SynRM-based laboratory demonstrator, including current ripple maps and torque ripple measurements.

The paper is organized as follows. Section II describes the integrated charging system, the SynRM model, the zero-torque current-reference selection, and the loss-oriented selection of the charger-side voltage. Section III analyzes the effect of the PWM carrier phase shift and machine nonlinearities on current and torque ripple. Section IV presents the control scheme of the integrated charger. Section V reports the experimental validation, and Section VI concludes the paper.

This work is licensed under a Creative Commons Attribution-NonCommercial-NoDerivatives 4.0 License.
For more information, see https://creativecommons.org/licenses/by-nc-nd/4.0/

This article has been accepted for publication in IEEE Transactions on Power Electronics. This is the author's version which has not been fully edited and content may change prior to final publication. Citation information: DOI 10.1109/TPEL.2026.3724067

TABLE I
COMPARISON WITH STATE-OF-THE-ART INTEGRATED CHARGING SOLUTIONS WITH DC/DC BOOST FUNCTIONALITY

Ref.	Charging type	Machine type	Boost DC/DC operation	Zero average torque	Loss-oriented v_{ch} selection	Current ripple analysis	Torque ripple analysis	Experimental validation	Distinctive feature
[12]	DC/DC charging operation	IPM	Yes, analyzed	Not addressed	No	Partial	Not addressed	FEM only	FEM-based evaluation of machine inductance and losses during charging operation
[13]	AC/DC and DC boost charging	Segmented PMSM	Yes	Yes	No	Partial	Yes	Yes	Integrated charger with enhanced winding filter inductance and zero-torque operation
[14]	Reconfigured OBC	PMSM	Yes	Suppressed by control	No	Partial	Yes	Yes	Analysis and suppression of rotational movement and charging torque
[23]	DC fast charging	Synchronous or induction machine	Yes, buck/boost	Not addressed	No	Not addressed	Not addressed	Yes	Drivetrain-integrated DC fast charger with buck/boost and bidirectional power transfer
[24]	DC boost charging	IPMSM	Yes	Yes, with position control	Efficiency improvement, not v_{ch}-based	Yes	Not mapped	Yes, reduced scale	Two-phase DC charging using differential-mode inductance for improved efficiency and zero torque
This work	DC/DC boost charging	SynRM	Yes	Yes, any rotor position	Yes, v_{ch}-based	Yes, including PS and saturation	Yes, including PS and saturation	Yes, reduced scale	SynRM-based DC/DC boost charger with zero-average-torque control and current/torque ripple trade-off analysis

II. DESCRIPTION OF THE INTEGRATED CHARGING SYSTEM

DC fast chargers are designed to be connected directly to the vehicle battery terminals. Thus, the off-board charger behaves as a current source that receives the operating setpoint $i_{ch,ref}$ from the Battery Management System (BMS) of the vehicle via a standard communication protocol, while the voltage at the charger terminals is determined by the State of Charge (SoC) of the battery and its internal impedance. Therefore, the BMS adjusts the setpoint of the battery current in accordance with the selected charging strategy, which is a constant-current constant-voltage (CC-CV) profile in most cases [5].

In this paper, the integrated boost converter depicted in Fig. 1 is placed between the vehicle battery and the external power source to adapt the voltage level of the 400 V charging station to the 800 V vehicle. Thus, the traction inverter can actively control the voltage v_{ch} at the charger terminals, regardless of the battery SoC, whereas the DC charging station adjusts the average charging current i_{ch}.

In this scenario, the following essential requirements must be met to guarantee proper control of the charging process and the safe operation of the external DC charger and vehicle:

- The machine should produce zero average torque to prevent the vehicle from moving independently of the angular position of the rotor.
- The voltage at the off-board charger terminals v_{ch} must be regulated within the Safe Operating Area (SOA) of the traction inverter and the off-board charger.

Furthermore, other aspects deserve to be explored in depth to optimize the system performance:

- The output stage of the off-board charger includes capacitors designed to absorb mainly the switching current generated by the DC/DC itself. The charger does not expect the load (battery) to produce any additional current ripple. Therefore, in the proposed configuration, an extra filtering stage (capacitor C_{in} in Fig. 1) must be introduced on the vehicle side to minimize the current ripple injected toward the off-board charger by the vehicle.
- The Phase Shift (PS) between the carriers of the PWM modulators of the traction inverter affects the current ripple on the phase connected to the off-board charger and the torque ripple. An accurate selection of the PS can reduce the current ripple, the size of the additional input capacitor, and the vibration and noise generated by the machine.
- The overall efficiency of the integrated charger, including machine and inverter losses, should be maximized.

The following sections present an analytical model of the system, which is then followed by an analysis of control and optimization aspects of the integrated charger.

A. Model of the SynRM

The machine shown in Fig. 1 can be regarded as a coupled boost inductor of a two-phase boost converter that adapts the power supplied by the DC charging station (low voltage level) to the vehicle battery (high voltage level). It is worth noting that the configuration of the machine windings precludes the circulation of a homopolar current component. Thus, the behavior of the machine can be fully described by applying the following linear transformations to the phase quantities of the machine (voltages, currents, and flux linkages):

This work is licensed under a Creative Commons Attribution-NonCommercial-NoDerivatives 4.0 License.
For more information, see https://creativecommons.org/licenses/by-nc-nd/4.0/

This article has been accepted for publication in IEEE Transactions on Power Electronics. This is the author's version which has not been fully edited and content may change prior to final publication. Citation information: DOI 10.1109/TPEL.2026.3724067

$$\bar{y}^S = \frac{2}{3}(x_1 + x_2\bar{\alpha} + x_3\bar{\alpha}^2) \quad (1)$$

$$\bar{y} = \bar{y}^S e^{-j\vartheta}. \quad (2)$$

In (1), $\bar{y}^S$ is the space vector in the natural (stationary) reference frame of three generic time-varying real quantities x_1, x_2, and x_3, while $\bar{\alpha}$ is a complex number equal to $e^{j2\pi/3}$. Also, $\bar{y}$ in (2) represents the space vector $\bar{y}^S$ seen from a generic d-q reference frame with the d-axis oriented in the direction of the generic vector $e^{j\vartheta}$. Equations (1) and (2) are commonly known as Clarke and Park transformations, respectively.

Transformations (1)-(2) can be applied to the phase voltage and flux equations of a SynRM, leading to the following well-known set of equations:

$$\bar{v}_S = R_S\bar{\imath}_S + \frac{d\bar{\varphi}_S}{dt} + j\omega\bar{\varphi}_S \quad (3)$$

$$\bar{\varphi}_S = \varphi_{Sd} + j\varphi_{Sq} = L_{Sd}i_{Sd} + jL_{Sq}i_{Sq}. \quad (4)$$

In (3)-(4), $\bar{v}_S$, $\bar{\imath}_S$, and $\bar{\varphi}_S$ are the space vectors of the stator voltages, currents, and flux linkages, respectively. The dynamics of the motor depends on the winding resistance R_S and the stator flux linkage $\bar{\varphi}_S$, which can be expressed in terms of $\varphi_{Sd}(i_{Sd}, i_{Sq})$ and $\varphi_{Sq}(i_{Sd}, i_{Sq})$, or by introducing the direct and quadrature apparent inductances $L_{Sd}(i_{Sd}, i_{Sq})$ and $L_{Sq}(i_{Sd}, i_{Sq})$. The electric angular position ϑ, used in (2) to derive (3)-(4), identifies the axis of the rotor geometry with the highest magnetic reluctance, leading to $L_{Sd} < L_{Sq}$. Lastly, ω is the electric angular speed of the rotor.

The machine model is then completed by the simplified expression of the torque generated by the interaction between the stator currents and the magnetic saliency of the rotor as follows:

$$T = \frac{3}{2}p(j\bar{\varphi}_S)\cdot\bar{\imath}_S = \frac{3}{2}p\left(L_{Sd} - L_{Sq}\right)i_{Sd}i_{Sq} \quad (5)$$

where p is the number of pole pairs of the machine.

B. Control of the voltage v_{ch} of the off-board charger

The analysis of the diagram in Fig. 1 leads to the conclusion that, at a steady state, the voltage v_{ch} is constant when the average values of the phase current i_{S3} and the charger current i_{ch} are equal to each other. However, to actively control v_{ch}, it is essential to ensure a temporary mismatch between the machine phase current i_{S3} and the charger current i_{ch}:

$$\frac{dv_{ch}}{dt} = \frac{i_{ch} - i_{S3}}{C_{in}} \quad (6)$$

where C_{in} is the decoupling capacitance between the off-board charger and the vehicle. Therefore, the current i_{S3} is the control variable used to adjust v_{ch}. This control choice introduces a constraint to the machine current vector $\bar{\imath}_S^S$. In fact, the inverse Clarke transformation of (1) applied to $\bar{\imath}_S^S$ leads to:

$$\begin{cases} \bar{\imath}_S^S \cdot 1 \equiv i_{S1} \\ \bar{\imath}_S^S \cdot \bar{\alpha} \equiv i_{S2} \\ \bar{\imath}_S^S \cdot \bar{\alpha}^2 \equiv i_{S3} \end{cases}. \quad (7)$$

where "·" represents the dot product operator between complex vectors. The practical consequence of the last constraint of (7) is graphically represented in Fig. 2. The projection of $\bar{\imath}_S^S$ on the axis $\bar{\alpha}^2$ must be equal to the control variable i_{S3}. In other words, $\bar{\imath}_S^S$ must lie on any point of the solid black line depicted in Fig. 2.

C. Zero torque generation constraint

Among the possible configurations of $\bar{\imath}_S^S$ that satisfy (7), the most interesting ones are those that produce no torque. Therefore, according to (5), i_{Sd} or i_{Sq} must be equal to zero. By analyzing the vector diagram in Fig. 2, two possible solutions can be identified:

$$T = 0 \Rightarrow \begin{cases} i_{Sd,ref} = 0 \\ i_{Sq,ref} = \dfrac{i_{S3,ref}}{\sin\vartheta_3} \end{cases} \quad (8)$$

$$T = 0 \Rightarrow \begin{cases} i_{Sd,ref} = \dfrac{i_{S3,ref}}{\cos\vartheta_3} \\ i_{Sq,ref} = 0 \end{cases} \quad (9)$$

where ϑ_3 is

$$\vartheta_3 = \frac{4}{3}\pi - \vartheta. \quad (10)$$

Solutions (8) and (9) are functions of ϑ_3, which can vary depending on the standstill position ϑ of the rotor. A viable criterion for selecting either (8) or (9) can be based on the minimization of the magnitude of the current vector $\bar{\imath}_S$, with the objective of reducing the machine Joule losses. The selection of the minimum magnitude of $\bar{\imath}_S$ is shown in Fig. 3. It can be noted that $|\bar{\imath}_{S,ref}|/|i_{3,ref}|$ ranges from 1 to $\sqrt{2}$ in the worst rotor angular position. In practical implementations, the transition between (8) and (9) should not be performed by an ideal discontinuous selector. Around the angular positions where the two solutions provide the same current magnitude, a hysteresis band can be introduced to avoid repeated commutations caused by rotor-position measurement noise. This implementation preserves the zero-average-torque condition because the selected current reference always belongs either to the d-axis or to the q-axis solution. Since the charging process is performed at standstill, the transition occurs only when the initial rotor position lies close to a sector boundary.

D. Inverter pole voltages and linear modulation area

Relationships (8)-(9) allow the direct calculation of $i_{Sd,ref}$ and $i_{Sq,ref}$ once the proper value of the phase current i_{S3} is selected. Therefore, a standard vector control scheme for synchronous machines based on PI controllers implemented on the d-q synchronous reference frame can be used, as shown in

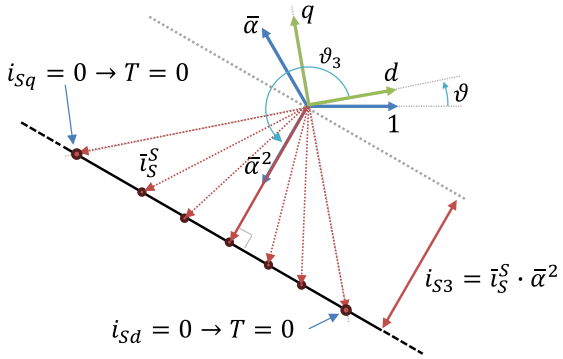

Fig. 2. Possible configurations of the current vector $\bar{\imath}_S^S$ that lead to the same current i_{S3}.

This work is licensed under a Creative Commons Attribution-NonCommercial-NoDerivatives 4.0 License.
For more information, see https://creativecommons.org/licenses/by-nc-nd/4.0/

This article has been accepted for publication in IEEE Transactions on Power Electronics. This is the author's version which has not been fully edited and content may change prior to final publication. Citation information: DOI 10.1109/TPEL.2026.3724067

the control scheme of Fig. 11 (an extended analysis can be found in Section IV). The reference voltage components $v_{Sd,ref}$ and $v_{Sq,ref}$ of the PI controllers are then combined in $\bar{v}_{S,ref}$ and converted into $\bar{v}^S_{S,ref}$ in the stationary reference frame through the inverse Park transformation. The last step of the control scheme is the calculation of the reference pole voltages $v_{10,ref}$ and $v_{20,ref}$ for the inverter legs. It is well known that, in three-phase drives, the voltage vector of the machine phase voltages equals that of the pole voltage ($\bar{v}^S_p$) generated by the inverter as follows:

$$\bar{v}^S_{S,ref} = \bar{v}^S_{P,ref} = \frac{2}{3}\left(v_{10,ref} + v_{20,ref}\bar{\alpha} + v_{30,ref}\bar{\alpha}^2\right). \quad (11)$$

Equation (11) can be adapted to the current case study by recalling that $v_{30,ref}$ is directly imposed by the charger voltage and that $\bar{v}^S_{S,ref}$ can be separated in the real and imaginary contributions $v^S_{S\alpha,ref} + jv^S_{S\beta,ref}$. Therefore, (11) becomes:

$$v^S_{S\alpha,ref} + jv^S_{S\beta,ref} = \frac{2}{3}\left(v_{10,ref} + v_{20,ref}\bar{\alpha} + v_{ch}\bar{\alpha}^2\right) \quad (12)$$

Solving the complex equation (12) for $v_{10,ref}$ and $v_{20,ref}$ one finds:

$$v_{20,ref} = \sqrt{3}v^S_{S\beta,ref} + v_{ch} \quad (13)$$

$$v_{10,ref} = \frac{1}{2}\left(3v^S_{S\alpha,ref} + v_{20,ref} + v_{ch}\right). \quad (14)$$

Equations (13) - (14) can be regarded as the reference pole voltages that the PWM modulators should synthesize in each switching period ($T_{sw} = 1/f_{sw}$) to impose the machine voltage $\bar{v}^S_{S,ref}$. Since the PWM modulation acts on the average voltage synthesized in the period T_{sw}, the instantaneous voltage applied by each inverter leg can only be equal to zero or v_{bat}. By introducing the leg binary switching functions s_1 and s_2, the instantaneous pole voltages become:

$$\begin{cases} v_{10} = s_1 v_{bat} & s_1 = 0,1 \\ v_{20} = s_2 v_{bat} & s_2 = 0,1 \end{cases} \quad (15)$$

Combining (15) and (12), one finds the instantaneous voltage vectors applied to the machine windings:

$$\bar{v}^S_S = \frac{2}{3}(s_1 v_{bat} + s_2 v_{bat}\bar{\alpha}) + \frac{2}{3}v_{ch}\bar{\alpha}^2. \quad (16)$$

Figure 4 shows the graphical representation of (16). The reference voltage $\bar{v}^S_{S,ref}$ must be within the green area in the picture, which represents the linear modulation area of the converter. The area depends on the off-board charger and battery voltages v_{ch} and v_{bat}.

E. Loss analysis and selection of the voltage reference v_{ch}

Off-board DC chargers are designed to be connected directly to the battery of the vehicle. Therefore, the charging voltage v_{ch} is mainly determined by the battery SoC and by the voltage drops across the battery internal impedance, the cables, and the connectors. As a result, the off-board charger typically operates as a current-controlled source and tracks the charging-current reference $i_{ch,ref}$ requested by the vehicle BMS.

Conversely, when the electric drivetrain is used as an integrated boost charger, the charger-side voltage v_{ch} and the battery-side voltage v_{bat} are decoupled by the boost operation of the integrated converter. Under steady-state conditions, the machine phase current involved in the charging process satisfies $i_{S3} = i_{ch}$. By neglecting losses, the ideal power balance of the converter leads to:

$$i_{S3} = i_{ch,ref} \cong \frac{v_{bat}}{v_{ch}} i_{bat} = \frac{i_{bat}}{m} \quad (17)$$

where i_{bat} denotes the magnitude of the battery-side charging current and $m = v_{ch}/v_{bat}$ is the voltage ratio of the integrated charger. Equation (17) shows that, for a given battery-side current i_{bat}, increasing m, i.e., increasing the charger-side voltage v_{ch}, reduces the machine charging current. This is beneficial because the machine winding losses and the inverter conduction losses are directly related to the currents flowing through the stator windings and the inverter legs.

To further clarify this point, the total power loss P_T of the integrated charger can be expressed by neglecting the machine iron losses and the phase current ripple, as follows:

$$P_T = P_{JS} + P_{Q1} + P_{Q2} \quad (18)$$

$$P_{JS} = \frac{3}{2}R_S|\bar{i}^S_S|^2 \quad (19)$$

$$P_{Q1} = P_{c,Q1} + P_{s,Q1} \quad (20)$$

$$P_{Q2} = P_{c,Q2} + P_{s,Q2} \quad (21)$$

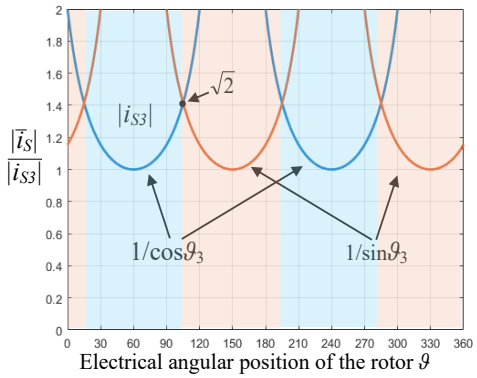

Fig. 3. Magnitude of the current vector $\bar{\imath}_S$ with respect to the charging current i_{S3} when the generated torque is zero.

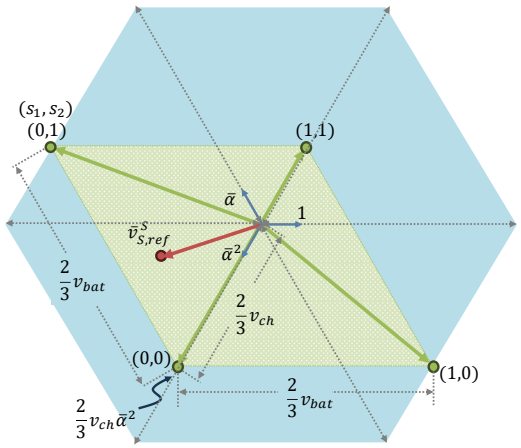

Fig. 4. Linear modulation regions of the inverter used for traction (blue area) and integrated charger (green area).

This work is licensed under a Creative Commons Attribution-NonCommercial-NoDerivatives 4.0 License.
For more information, see https://creativecommons.org/licenses/by-nc-nd/4.0/

This article has been accepted for publication in IEEE Transactions on Power Electronics. This is the author's version which has not been fully edited and content may change prior to final publication. Citation information: DOI 10.1109/TPEL.2026.3724067

where P_{JS} represents the stator Joule losses, while P_{Q1} and P_{Q2} are the losses of the two active inverter legs, including both conduction and switching contributions. These inverter legs are composed of the transistor pairs $Q_{1H}-Q_{1L}$ and $Q_{2H}-Q_{2L}$ respectively. Assuming constant phase currents i_{S1} and i_{S2}, within one switching period, the inverter-leg losses can be approximated as:

$$P_{Q1} = R_{on} i_{S1}^2 + V_{th}|i_{S1}| + \tau_{sw} v_{bat} |i_{S1}| f_{Sw} \quad (22)$$

$$P_{Q2} = R_{on} i_{S2}^2 + V_{th}|i_{S2}| + \tau_{sw} v_{bat} |i_{S2}| f_{Sw}. \quad (23)$$

In (22) and (23), V_{th} and R_{on} are the equivalent threshold voltage and on-state resistance of the inverter semiconductor devices, including the contribution of the transistors and antiparallel diodes. The parameter τ_{sw} represents the equivalent duration of the turn-on and turn-off switching intervals.

From (19), (22), and (23), together with (7) and (17), it can be observed that the main loss contributions depend on the voltage ratio through terms proportional to $1/m$ and $1/m^2$. Therefore, increasing m reduces the machine and inverter currents and, consequently, improves the efficiency of the integrated charger. This analysis suggests that, within the voltage and modulation limits of the converter, the charger-side voltage v_{ch} should be kept as high as possible, thus minimizing the required charging-current reference $i_{ch,ref}$.

To support this analytical consideration, numerical simulations were carried out. The machine parameters and converter loss characteristics were selected according to the components and operating conditions used for the experimental validation presented in Section V. The model was implemented in Plexim PLECS and includes the control algorithm described in Section IV, the machine model, and the conduction and switching loss models of the semiconductor devices used in the laboratory prototype.

The losses and overall system efficiency were mapped as functions of the rotor electrical position ϑ and voltage ratio m. The simulations were performed with $v_{bat} = 200\,V$, $i_{bat} = 10A$, an inverter switching frequency of 10 kHz, and a semiconductor junction temperature fixed at 125 °C. The loss maps reported in Fig. 5 were obtained by considering the worst-case carrier phase shift in terms of average losses. Additional simulations showed that the influence of PS on the average efficiency is significantly smaller than the effect of the voltage ratio m and rotor position. Therefore, PS is mainly treated as a degree of freedom for current- and torque-ripple mitigation, as discussed in Section III, rather than as a primary variable for average-loss minimization.

Fig. 5 shows that the losses of the integrated charger depend on the standstill rotor position, consistently with the zero-torque current selection discussed in Section II.C. This dependence is mainly caused by the different current amplitudes required by (8) and (9) at different rotor positions. Nevertheless, the dominant trend is governed by the voltage ratio m. As m increases, the required charger current $i_{ch,ref}$ decreases according to (17), thus reducing both the machine Joule losses and the inverter losses. Consequently, the integrated charger efficiency increases with m in the operating range investigated. These results support the analytical conclusion that the off-board charger voltage v_{ch} should be set to the highest permissible value compatible with the converter voltage limits and the charging operating conditions.

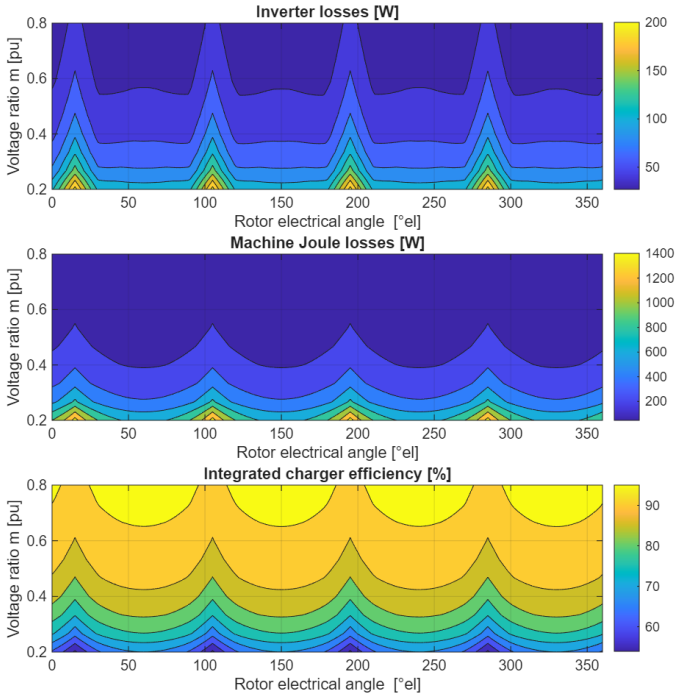

Fig. 5. Steady-state efficiency and loss maps of the integrated charger as functions of rotor electrical position and voltage ratio, with $v_{bat} = 200$ V and $i_{bat} = 10$ A.

III. Torque and Current Ripple Analysis

The PS between the carriers of the leg modulators affects the current ripple of the phase connected to the off-board charger and the residual torque ripple at the shaft (the average torque is zero, as discussed in Section II.C).

To investigate the problem analytically, the system can be analyzed at a steady state considering $\omega = 0$ (locked rotor) for a fixed rotor position ϑ. Furthermore, due to the boost nature of the charger, the machine quantities can be separated in the DC contributions $\bar{v}_{S,ref}$, $\bar{\imath}_{S,ref}$ and $\bar{\varphi}_{S,0}$ ($\bar{v}_{S,ref}$, $\bar{\imath}_{S,ref}$ are reference voltage and current requested in a switching period T_{sw} by the control algorithm), and AC components $\tilde{v}_{S,AC}$, $\tilde{\imath}_{S,AC}$, and $\tilde{\varphi}_{S,AC}$ induced by the PWM.

$$\bar{v}_S = \bar{v}_{S,ref} + \tilde{v}_{S,AC} \quad (24)$$

$$\bar{\imath}_S = \bar{\imath}_{S,ref} + \tilde{\imath}_{S,AC} \quad (25)$$

$$\bar{\varphi}_S = \bar{\varphi}_{S,0} + \tilde{\varphi}_{S,AC} \quad (26)$$

Introducing (24)-(26) into the machine equations (3)-(4) and separating the DC terms from the AC terms, one finds:

$$\bar{v}_{S,ref} = R_S \bar{\imath}_{S,ref} \quad (27)$$

$$\tilde{v}_{S,AC} = R_S \tilde{\imath}_{S,AC} + \frac{d\tilde{\varphi}_{S,AC}}{dt} \quad (28)$$

Equation (27) states that $\bar{v}_{S,ref}$ sustains the voltage drop of the DC current contribution $\bar{\imath}_{S,ref}$ on the machine resistance R_S, and (28) describes the evolution of the current and flux ripple of the machine. It is worth noting that the time derivative of the flux for a nonlinear machine depends on the current bias $\bar{\imath}_{S,ref}$, leading to:

This work is licensed under a Creative Commons Attribution-NonCommercial-NoDerivatives 4.0 License.
For more information, see https://creativecommons.org/licenses/by-nc-nd/4.0/

This article has been accepted for publication in IEEE Transactions on Power Electronics. This is the author's version which has not been fully edited and content may change prior to final publication. Citation information: DOI 10.1109/TPEL.2026.3724067

$$\frac{d\bar{\varphi}_{S,AC}}{dt} = \left(\frac{\partial \varphi_{Sd}}{\partial i_{Sd}} + j\frac{\partial \varphi_{Sq}}{\partial i_{Sd}}\right)\frac{di_{Sd,AC}}{dt} + \left(\frac{\partial \varphi_{Sd}}{\partial i_{Sq}} + j\frac{\partial \varphi_{Sq}}{\partial i_{Sq}}\right)\frac{di_{Sq,AC}}{dt}. \quad (29)$$

The four partial derivatives of the flux in (29) can be interpreted as differential inductances, composed of two self-contributions ($\mathcal{L}_{Sdd}$ and $\mathcal{L}_{Sqq}$) and two d-q coupling terms ($\mathcal{L}_{Sdq}$ and $\mathcal{L}_{Sqd}$) as follows:

$$\begin{aligned}\mathcal{L}_{Sdd}(\bar{\imath}_{S,ref}) &= \frac{\partial \varphi_{Sd}}{\partial i_{Sd}}\\ \mathcal{L}_{Sdq}(\bar{\imath}_{S,ref}) &= \frac{\partial \varphi_{Sd}}{\partial i_{Sq}}\\ \mathcal{L}_{Sqq}(\bar{\imath}_{S,ref}) &= \frac{\partial \varphi_{Sq}}{\partial i_{Sq}}\\ \mathcal{L}_{Sqd}(\bar{\imath}_{S,ref}) &= \frac{\partial \varphi_{Sq}}{\partial i_{Sd}}\end{aligned} \quad (30)$$

The maps of the d-q flux linkages, the differential inductances, the torque characteristic, and the rotor lamination of the reference SynRM used in the following analysis and the experimental section are reported in Fig. 6 and Fig. 7. The results have been obtained by means of numerical finite element analysis. Figure 6 suggests that the cross-coupling inductances $\mathcal{L}_{Sdq}$ and $\mathcal{L}_{Sqd}$ are smaller than the self-contributions $\mathcal{L}_{Sdd}$ and $\mathcal{L}_{Sqq}$. Thus, by neglecting $\mathcal{L}_{Sdq}$ and $\mathcal{L}_{Sqd}$, the d-axis and q-axis ripple dynamics can be decoupled, and (28) can be simplified as follows:

$$\bar{v}_{S,AC} = R_S\bar{\imath}_{S,AC} + \mathcal{L}_{Sdd}\frac{di_{Sd,AC}}{dt} + j\mathcal{L}_{Sqq}\frac{di_{Sq,AC}}{dt}. \quad (31)$$

Once the parameters of the machine and $\bar{v}_{S,AC}$ are known, the current ripple $\bar{\imath}_{S,AC}$ in (31) can be calculated. To simplify the calculation of $\bar{v}_{S,AC}$, the resistive voltage drop in (27) can be neglected, leading to the following result:

$$\bar{v}_{S,ref} = \bar{v}^{S}_{S,ref}e^{-j\vartheta} = R_S\bar{\imath}_{S,ref} \cong 0. \quad (32)$$

Introducing (32) into (24), and considering (16), one finds the final expression of the voltage ripple $\bar{v}_{S,AC}$ as follows:

$$\bar{v}_{S,AC} = \frac{2}{3}[s_1(t)v_{bat} + s_2(t)v_{bat}\bar{\alpha} + v_{ch}\bar{\alpha}^2]e^{-j\vartheta}. \quad (33)$$

The modulation strategy of the converter is defined by the instantaneous evolution of s_1 and s_2 within the switching period T_{sw}. Thus, infinite combinations of $s_1(t)$ and $s_2(t)$ are suitable for controlling the average voltage of the converter as long as (32) is satisfied. Introducing (12) in (32), one finds the values of the reference pole voltages $v_{10,ref}$ and $v_{20,ref}$, and the

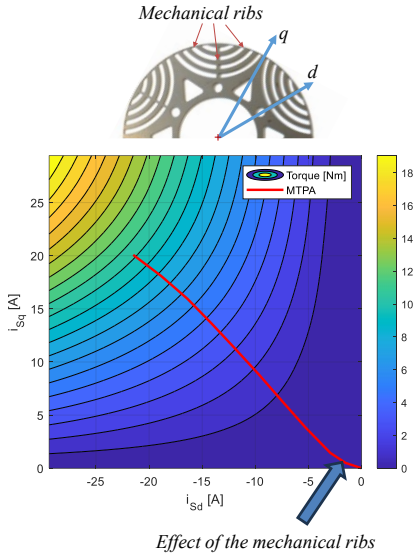

Fig. 7. Torque characteristic and MTPA locus of the reference machine as a function of i_{Sd} and i_{Sq}. Detail of the rotor lamination.

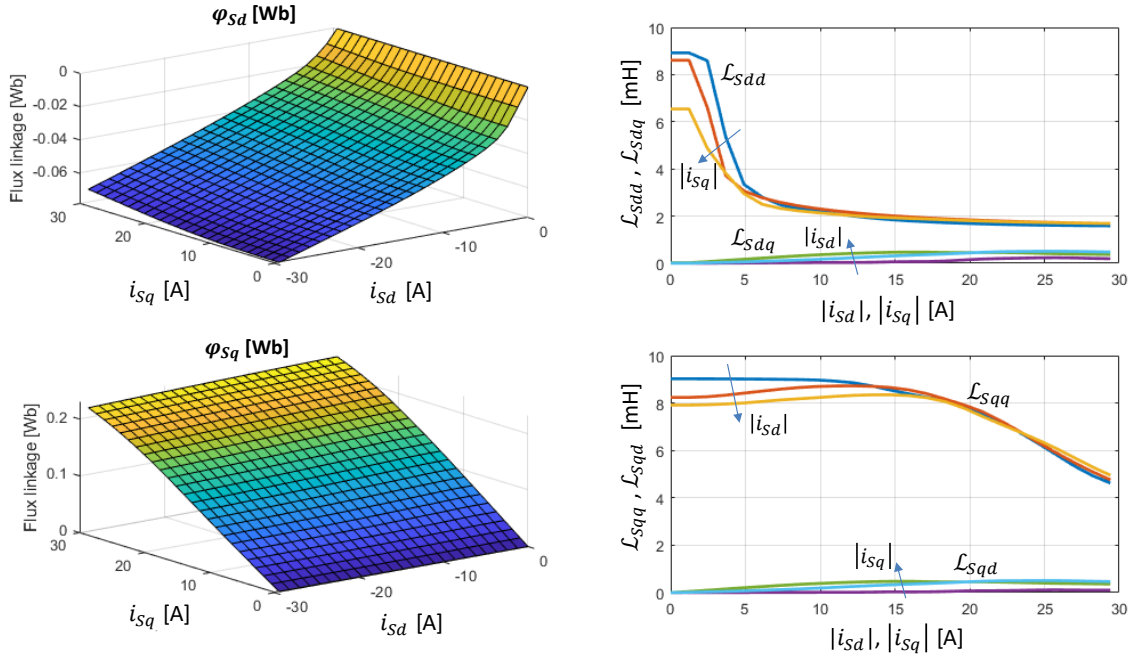

Fig. 6. Flux linkage components φ_{Sd} and φ_{Sq} as a function of i_{Sd} and i_{Sq} for the reference machine. Differential inductances $\mathcal{L}_{Sdd}$, $\mathcal{L}_{Sqq}$ (self-contributions), and $\mathcal{L}_{Sdq}$, $\mathcal{L}_{Sqd}$ (cross-coupling terms).

This work is licensed under a Creative Commons Attribution-NonCommercial-NoDerivatives 4.0 License.
For more information, see https://creativecommons.org/licenses/by-nc-nd/4.0/

This article has been accepted for publication in IEEE Transactions on Power Electronics. This is the author's version which has not been fully edited and content may change prior to final publication. Citation information: DOI 10.1109/TPEL.2026.3724067

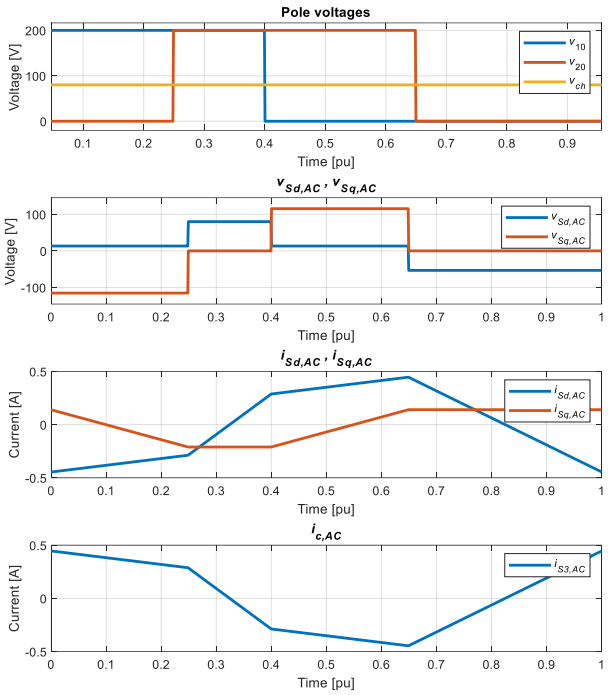

Fig. 8. Current ripple analysis when $\frac{v_{ch}}{v_{bat}} = 0.4$, $\vartheta = 100\,°el$, and the phase shift between the carriers is 0.25 pu.

relationship with the switching functions $s_1(t)$ and $s_2(t)$:

$$v_{10,ref} = v_{20,ref} = v_{ch} \tag{34}$$

$$\int_{T_{sw}} s_1(t) v_{bat} dt = \int_{T_{sw}} s_2(t) v_{bat} dt = v_{ch}. \tag{35}$$

This paper considers only PWM strategies with a single pulse per switching period. Therefore, the only degree of freedom that makes $s_1(t)$ and $s_2(t)$ different is the PS between the carriers of the PWM. The PS in this analysis is expressed as a per-unit number with respect to the switching period T_{sw}. The current ripple components $i_{Sd,AC}$ and $i_{Sq,AC}$ can finally be obtained from (31) and (33) for a given PS. Once $\bar{\imath}_{S,AC}$ is known, the current ripple $i_{S3,AC}$ can be derived through (7).

As an example, Fig. 8 shows the result of the numerical calculation considering a voltage ratio m of 0.4, a rotor angular position ϑ of 100° (electrical degrees), a charging current $i_{ch,ref}$ of 5 A, and a phase shift of 0.25 pu between the carriers. The battery voltage v_{bat} is set to 200 V, and the switching frequency is set to 10 kHz in accordance with the experimental test scenario presented in Section V. The figure shows the theoretical waveforms of the pole voltages, the d-q components of $\bar{v}_{S,AC}$, the d-q components of the current ripple $\bar{\imath}_{S,AC}$, and $i_{S3,AC}$ at the switching-period time scale.

The previous calculations can be extended to any electric angular position $\vartheta \in [0, 2\pi]$ and any variable phase shift $\in [0, 0.5]$ pu. The results of the calculation, considering a voltage ratio m of 0.5, and a charger current $i_{ch,ref}$ of 0.5 A and 10 A, are reported in Fig. 9 and Fig. 10, respectively. The performance indicators used in the color maps are the peak-to-peak values of currents $i_{Sd,AC}$, $i_{Sq,AC}$, $i_{S3,AC}$, and the product between i_{Sd} and i_{Sq}. The comparison of the two figures demonstrates that the magnetic saturation of the machine influences the ripple. In fact, at low values of $i_{ch,ref}$, the differential inductances $\mathcal{L}_{Sdd}$ and $\mathcal{L}_{Sqq}$ are nearly equal as illustrated in Fig. 6. This behavior is due to the mechanical ribs that connect the rotor flux barriers as highlighted in Fig. 6. In fact, a minimum level of i_{Sd} is required to saturate the ribs and enhance the rotor saliency. Thus, at low currents, the d- and q-axis reluctances are almost equal. This characteristic can also be appreciated in the shape of the MTPA curve of the machine

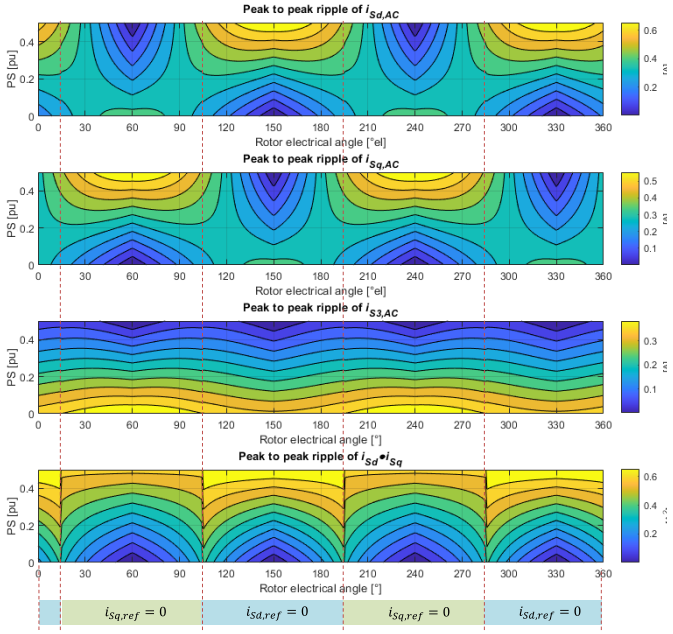

Fig. 9. Peak to peak ripple of $i_{Sd,AC}$, $i_{Sq,AC}$, $i_{S3,AC}$ and $i_{Sd}i_{Sq}$ as a function of the rotor electrical angle and carrier phase shift when $i_{ch,ref} = 0.5$ A.

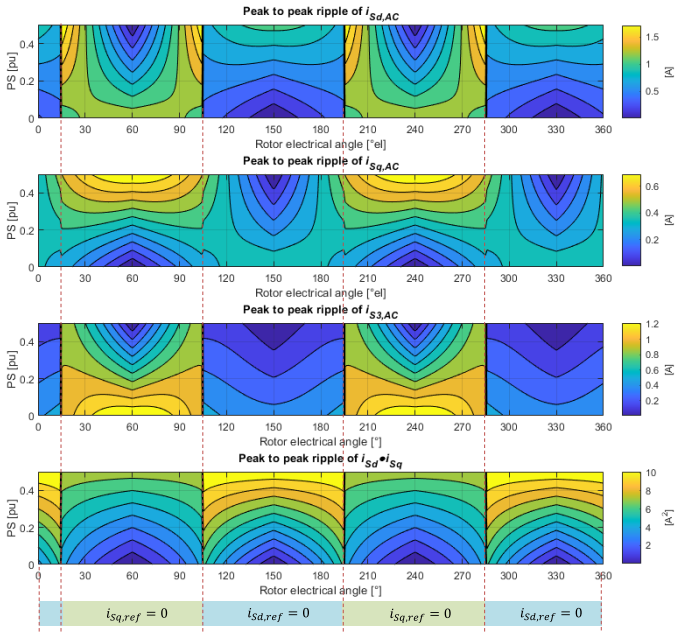

Fig. 10. Peak to peak ripple of $i_{Sd,AC}$, $i_{Sq,AC}$, $i_{S3,AC}$ and $i_{Sd}i_{Sq}$ as a function of the rotor electrical angle and carrier phase shift when $i_{ch,ref} = 10$ A.

This work is licensed under a Creative Commons Attribution-NonCommercial-NoDerivatives 4.0 License.
For more information, see https://creativecommons.org/licenses/by-nc-nd/4.0/

This article has been accepted for publication in IEEE Transactions on Power Electronics. This is the author's version which has not been fully edited and content may change prior to final publication. Citation information: DOI 10.1109/TPEL.2026.3724067

at low torque values.

In conclusion, Figs 9 and 10 suggest that the PS between the PWM carriers should be maintained at 0.5 pu, regardless of the angular position ϑ and magnetic saturation, if the main objective in the application is the minimization of the phase current ripple $i_{S3,AC}$.

However, a secondary aim of the integrated charger might be minimizing the torque ripple generated by the machine during the charging process to reduce vibrations and acoustic noise. The torque generated by the machine can be expressed by introducing (25) in (5) as follows:

$$T = \frac{3}{2} p \left(L_{Sd} - L_{Sq}\right)\left(i_{Sd,ref} + i_{Sd,AC}\right)\left(i_{Sq,ref} + i_{Sq,AC}\right) \quad (36)$$

Depending on the angular position of the rotor, the control system uses (8) or (9) to determine the current references $i_{Sd,ref}$ and $i_{Sq,ref}$ to produce no torque. Therefore, the dominant torque contributions in (36) can be simplified and separated as follows:

$$(8) \Rightarrow \begin{cases} i_{Sd,ref} = 0 \\ i_{Sq,ref} = \dfrac{i_{S3,ref}}{\sin \vartheta_3} \end{cases} \Rightarrow T \propto \frac{i_{S3,ref} i_{Sd,AC}}{\sin\left(\vartheta_3\right)} \quad (37)$$

$$(9) \Rightarrow \begin{cases} i_{Sd,ref} = \dfrac{i_{S3,ref}}{\cos \vartheta_3} \\ i_{Sq,ref} = 0 \end{cases} \Rightarrow T \propto \frac{i_{S3,ref} i_{Sq,AC}}{\cos\left(\vartheta_3\right)}. \quad (38)$$

Relations (37) and (38) indicate that the torque ripple in each angular sector of the rotor is proportional to $i_{Sd,AC}$ or $i_{Sq,AC}$. Thus, in order to minimize the torque ripple, the PS should be adjusted to minimize $i_{Sd,AC}$ or $i_{Sq,AC}$. This result is numerically verified by the last plots in Fig. 9 and Fig. 10. The figures clearly suggest that, independently of the rotor standstill position, a PS equal to zero minimizes the torque ripple.

In conclusion, the PS affects both the current ripple on i_{S3} (injected toward the off-board charger) and the residual torque ripple at the shaft. The two objectives cannot be minimized simultaneously, so a trade-off strategy is required. Therefore, a trade-off strategy should be implemented to limit both phenomena simultaneously.

IV. Control Scheme

Fig. 11 shows the control scheme of the proposed integrated boost converter. The control algorithm aims to charge the battery following a constant-current constant-voltage (CC-CV) profile. The actual current i_{bat} is indirectly controlled by the BMS by adjusting the current setpoint $i_{ch,ref}$ sent to the off-board charger through a standard communication protocol. Furthermore, the loss optimization strategy briefly discussed in Section II.E selects the most suitable value of $v_{ch,ref}$, i.e., the highest admissible value, and the PS between the modulators depending on the machine parameters, the angular position ϑ of the rotor, and the battery voltage level. The block denoted as "current controller and PS optimization" in Fig. 11 is implemented as a supervisory algorithm rather than as a high-bandwidth optimization loop.

The supervisory layer selects $v_{ch,ref}$ and PS according to two different criteria. The voltage reference $v_{ch,ref}$ is selected from the loss analysis of Section II.E. Since the average efficiency is mainly affected by the voltage ratio m, the highest admissible charger-side voltage is preferred, provided that the off-board charger voltage range, the battery voltage, and the inverter modulation limits are satisfied.

Conversely, PS is selected mainly to satisfy the ripple requirements of the application. The analysis of Section III shows that PS = 0.5 pu minimizes the current ripple of i_{S3}, whereas PS = 0 pu minimizes the residual torque ripple. Therefore, PS can be selected from precomputed maps or lookup tables according to the maximum admissible charger-side current ripple and torque ripple.

Once $v_{ch,ref}$ is selected, PI controller a) adjusts the current reference $i_{S3,ref}$ to regulate the voltage v_{ch} applied on the external charger. In addition, the reference current components $i_{Sd,ref}$ and $i_{Sq,ref}$ are calculated by using (8)-(9) and tracked by PI regulators b) and c).

The outputs of the d-q current controllers form the voltage vector $\bar{v}_{S,ref}$, which is then computed in the stationary reference frame with the inverse Park transformation. Finally, the

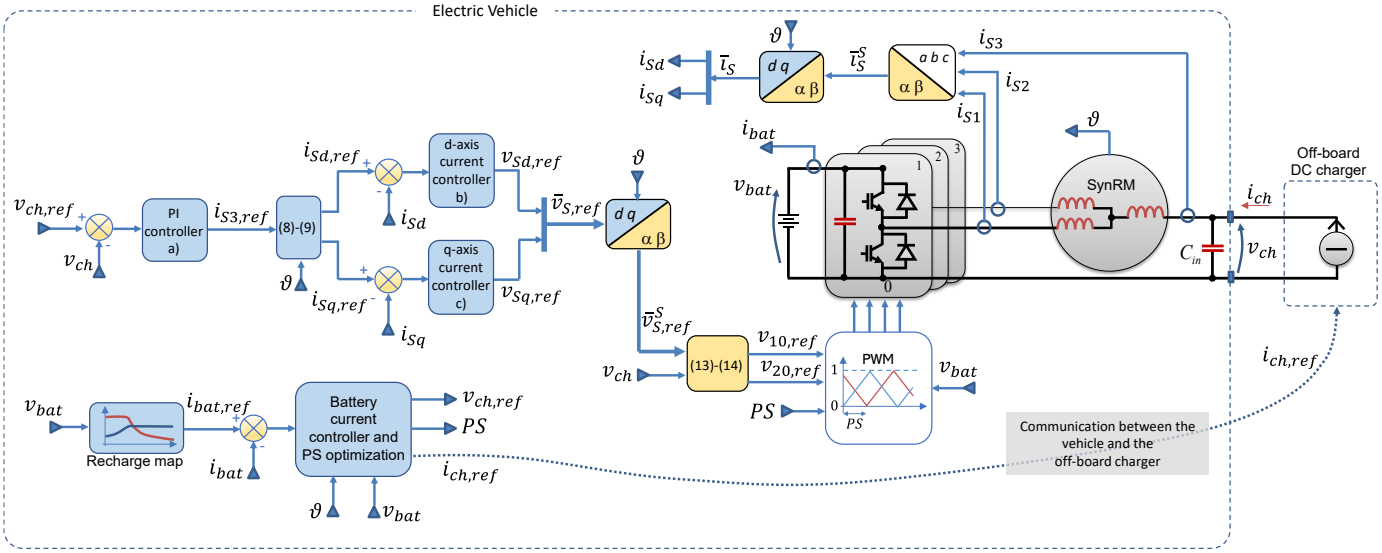

Fig. 11. Control scheme of the proposed integrated battery charger based on SynRM.

This work is licensed under a Creative Commons Attribution-NonCommercial-NoDerivatives 4.0 License.
For more information, see https://creativecommons.org/licenses/by-nc-nd/4.0/

This article has been accepted for publication in IEEE Transactions on Power Electronics. This is the author's version which has not been fully edited and content may change prior to final publication. Citation information: DOI 10.1109/TPEL.2026.3724067

reference pole voltages of the inverter are calculated by using (13) and (14).

V. Experimental Results

Experimental tests have been performed to verify the effectiveness of the proposed integrated battery charger and the current ripple analysis. The electrical and physical parameters of the SynRM are reported in Table II, while Fig. 12 shows the test setup and the rotor lamination of the motor. The traction inverter is a custom design based on the IGBT module Infineon IFS100B12N3E4_B31 controlled by a Texas Instruments TMS320F28335 microcontroller. The battery voltage v_{bat} is set to 200 V through a battery emulator Cinergia GE 20, while the off-board charger is represented by the DC power supply EA-PS 9500-20. The decoupling capacitance C_{in} placed between the off-board charger and the machine windings is equal to 820 µF. During the tests, the voltage v_{ch} is set to 100 V, while the switching frequency of the IGBT inverter is set to 10 kHz.

The PI gains used in the experimental tests are reported in Table III. The d- and q-axis current controllers were initially tuned by considering a nominal small-signal model of the SynRM at standstill, using the stator resistance and the nominal d and q-axis inductances reported in Table II. The gains were then refined experimentally to account for the digital implementation, inverter dead time, voltage saturation, and parameter variations due to magnetic saturation. The voltage controller of v_{ch} was tuned by considering the dynamics of the input capacitor C_{in}, where the phase current i_{S3} acts as the control variable for regulating the charger-side voltage. The voltage loop was selected slower than the inner current loops to preserve time-scale separation between the regulation of v_{ch} and the tracking of the d-q current references.

Figure 13 shows the effectiveness of the control scheme in regulating v_{ch} at the charger terminals. At time t_0, the setpoint of v_{ch} is increased from 70 V to 130 V while the charger current i_{ch} is 10 A. The control system temporarily reduces the phase current i_{S3} in order to charge the output capacitance C_{in} and adjust v_{ch}. At steady state, i_{S3} equals i_{ch}, and the duty cycle of the pole voltage v_{10} is proportional to the voltage ratio $m = v_{ch}/v_{bat}$.

Figure 14 provides additional insight into the control loop of

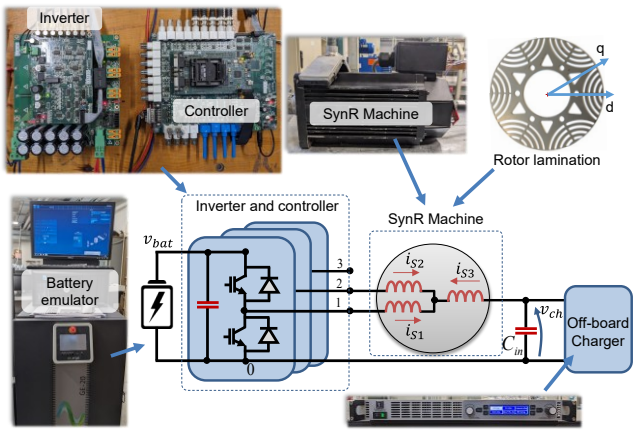

Fig. 12. Experimental setup of the integrated boost charger.

v_{ch}. At time t_0, i_{ch} is set to 10 A with a current slope of 100 A/s. During this transition, the controller is able to maintain the voltage v_{ch} at the setpoint of 100 V by increasing the current

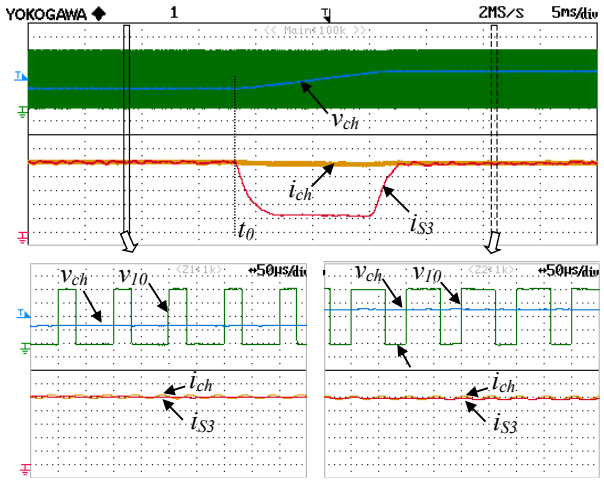

Fig. 13. Behavior of the system when the setpoint of v_{ch} changes from 70 V to 130 V and i_{ch} is set to 10 A. Waveforms of the charger current i_{ch}(2 A/div) and voltage v_{ch}(50 V/div), phase current i_{S3}(2 A/div), and pole voltage v_{10}(50 V/div).

TABLE II
PHYSICAL AND ELECTRICAL PARAMETERS OF THE SYNRM

Number of stator slots	36
Number of pole pairs	3
Number of slots per pole per phase (full-pitch winding)	2
Lamination material	M330-50A
Lamination active length	100 mm
Stator outer diameter	140 mm
Diameter at the airgap	80 mm
Number of flux barriers of the rotor	4
Flux barrier thickness	2 mm
Airgap thickness	0.5 mm
Machine rated current	$I_{S,rated} = 25\ \mathrm{A_{RMS}}$
Rated torque	$T_{rated} = 5$ Nm
Phase to neutral resistance (20 °C)	$R_S = 200$ mΩ
Rated d-axis inductance	$L_{Sd} = 2.9$ mH
Rated q-axis inductance	$L_{Sq} = 6.7$ mH

TABLE III
PARAMETERS OF THE PI REGULATORS

d-axis current controller (b)	$K_i = 300\ \mathrm{V/(A\,s)}$ $K_p = 0.017\ \mathrm{V/A}$
q-axis current controller (c)	$K_i = 300\ \mathrm{V/(A\,s)}$ $K_p = 0.04\ \mathrm{V/A}$
v_{ch} voltage controller(a)	$K_i = 6\ \mathrm{A/(V\,s)}$ $K_p = 1.2\ \mathrm{A/V}$

This work is licensed under a Creative Commons Attribution-NonCommercial-NoDerivatives 4.0 License.
For more information, see https://creativecommons.org/licenses/by-nc-nd/4.0/

This article has been accepted for publication in IEEE Transactions on Power Electronics. This is the author's version which has not been fully edited and content may change prior to final publication. Citation information: DOI 10.1109/TPEL.2026.3724067

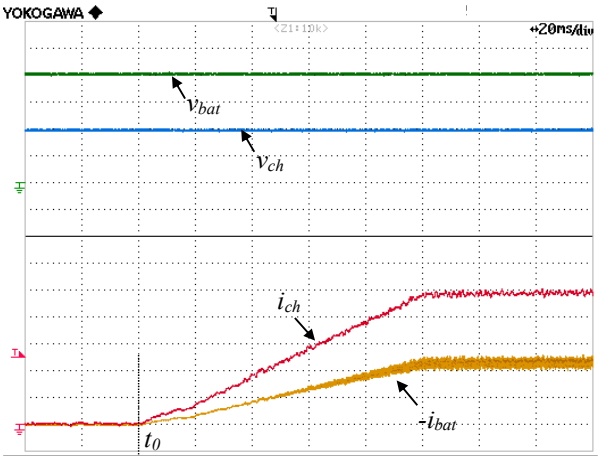

Fig. 14. Behavior of the system when the setpoint of i_{ch} changes from 0 A to 10 A at 100 A/s and v_{ch} is set to 100 V. Waveforms of the charger current i_{ch}(2 A/div) and voltage v_{ch}(50 V/div), battery current i_{bat}(2 A/div), and voltage v_{bat}(50 V/div).

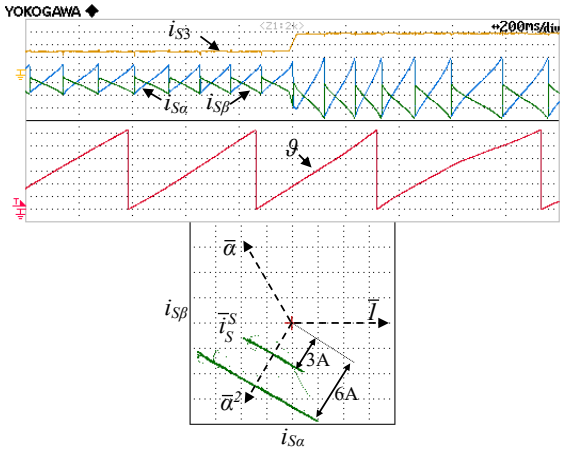

Fig. 15. Phase current i_{S3}, machine current vector $\bar{\imath}_S^S$ and its trajectory in the α-β plane as a function of the rotor angle ϑ. i_{S3} (2 A/div), $i_{S\alpha}$ (2 A /div), $i_{S\beta}$ (2 A /div), and ϑ (1 rad/div).

i_{S3}. As a result, the battery begins charging, and the current i_{bat} is approximately equal to -$i_{ch}m$.

Figure 15 aims to verify the constraint between the phase current i_{S3} and the current vector $\bar{\imath}_S^S$. The figure shows the input current i_{S3}, the components of the current vector $\bar{\imath}_S^S$ and its trajectory in the α-β plane as a function of the rotor angle ϑ. At time t_0, the setpoint of i_{S3} is increased from 3 A to 6 A. It can be noted that the control system can regulate the input current i_{S3} independently of the rotor position. Furthermore, the trajectory of $\bar{\imath}_S^S$ agrees with (7) and Fig. 2. The selection of $\bar{\imath}_{S,ref}$ follows the constraints (8)-(9) to generate zero torque on the shaft regardless of the actual rotor angle.

The effect of the phase shift between the pole voltages v_{10} and v_{20} on the current ripple of i_{S3} is shown in Fig. 16. The tests are performed with a current i_{ch} of 10 A, at the angular positions $\vartheta = 60°$ and $\vartheta = 90°$, and with phase shifts of 0.0 pu, 0.25 pu, and 0.5 pu. The predicted peak-to-peak current ripple attenuation in Fig. 10 agrees with the experimental results. Furthermore, it can be observed that the ripple of i_{S3} depends on ϑ and decreases as the PS increases.

The final experimental analysis aims to obtain the maps of the current ripple in low and high charging current conditions.

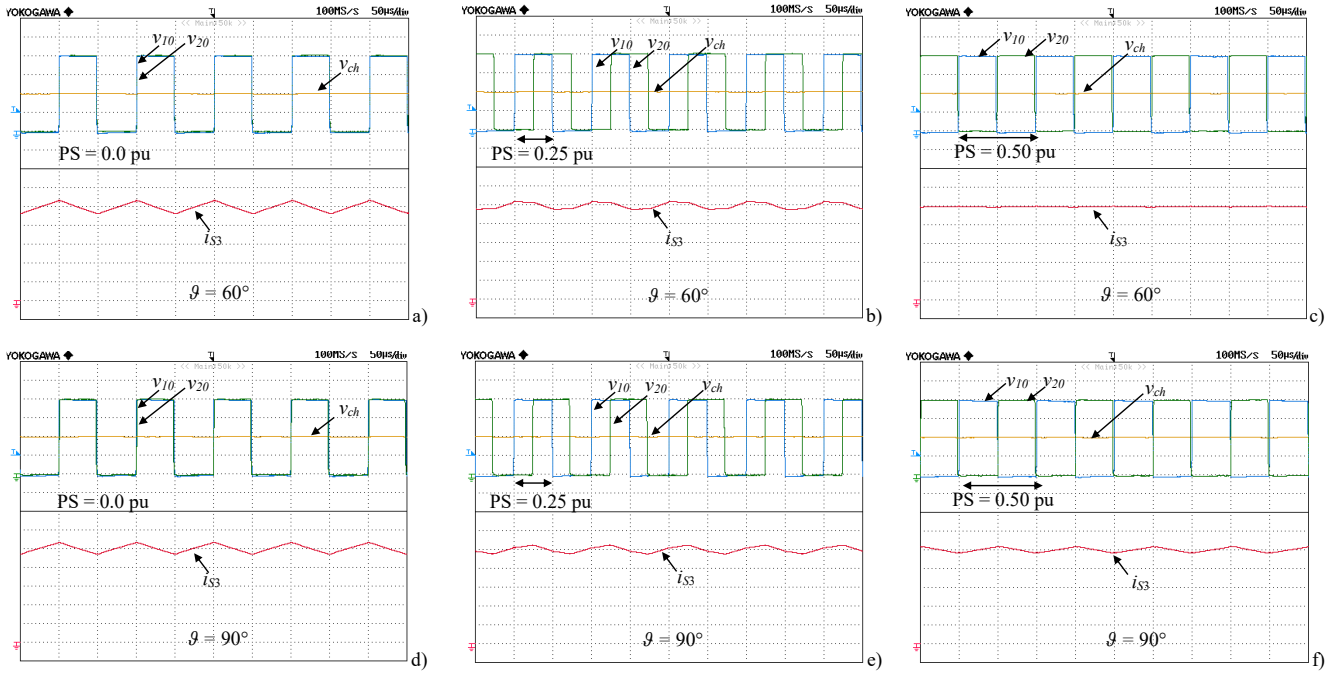

Fig. 16. Effect of the PS between the pole voltages v_{10} and v_{20} on the current ripple of i_{S3} for different rotor positions. Waveforms of v_{10} (50 V/div), v_{20} (50 V/div), v_{ch} (50 V/div), and i_{S3} (2 A/div).

This work is licensed under a Creative Commons Attribution-NonCommercial-NoDerivatives 4.0 License.
For more information, see https://creativecommons.org/licenses/by-nc-nd/4.0/

This article has been accepted for publication in IEEE Transactions on Power Electronics. This is the author's version which has not been fully edited and content may change prior to final publication. Citation information: DOI 10.1109/TPEL.2026.3724067

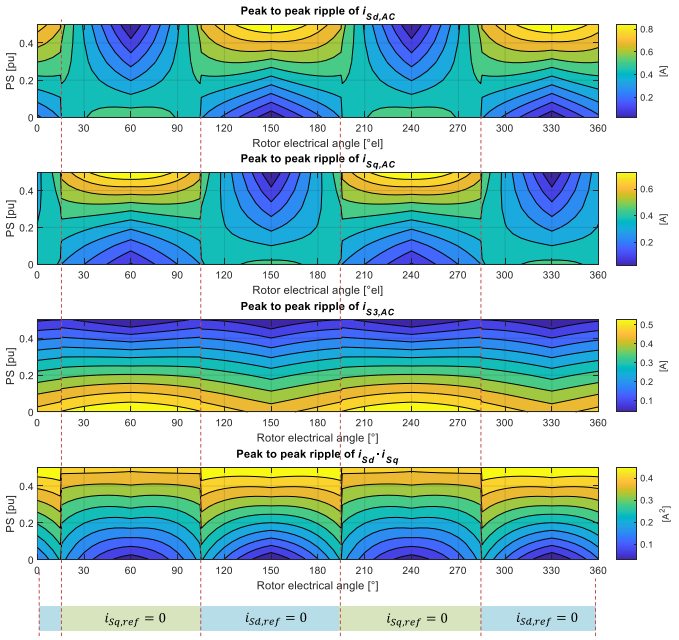

Fig. 17. Experimental evaluation of the peak to peak ripple of $i_{Sd,AC}$, $i_{Sq,AC}$, $i_{S3,AC}$ and $i_{Sd}i_{Sq}$ as a function of the rotor electrical angle and carrier phase shift PS when $i_{ch,ref}$ = 0.5 A.

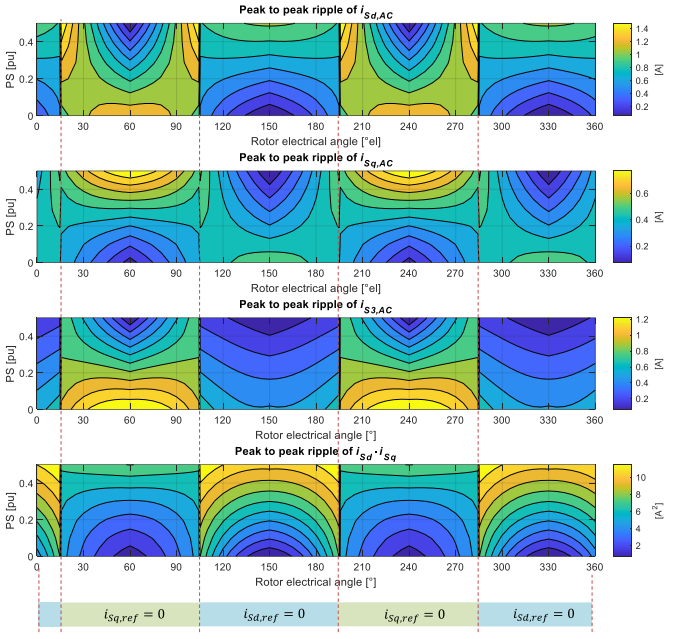

Fig. 18. Experimental evaluation of the peak to peak ripple of $i_{Sd,AC}$, $i_{Sq,AC}$, $i_{S3,AC}$ and $i_{Sd}i_{Sq}$ as a function of the rotor electrical angle and carrier phase shift PS when $i_{ch,ref}$ = 10 A.

Firstly, the waveforms of the phase currents i_{S1}, i_{S2}, and i_{S3} were acquired from 60° to 150° at 5° intervals, and the PS from 0 pu to 0.5 pu with a 0.1 step size, resulting in a total of 114 tested points. Then, the waveforms were imported into the MATLAB environment to calculate the instantaneous current vector $\bar{\imath}_S$ in the d-q reference frame and evaluate the average peak-to-peak current ripples of i_{S3}, i_{Sd}, i_{Sq}, and the torque product $i_{Sd}i_{Sq}$. Due to the expected symmetry of the maps shown in Figs. 9 and 10, the analysis of the angular interval 60° to 150° is sufficient to extract the behavior of the integrated charger over the entire 360°. The results of these tests are presented in Figs. 17 and 18 with a charging current $i_{ch,ref}$ equal to 0.5 A and 10 A, respectively. The obtained isolines of the ripple are in accordance with the theoretical ones shown in Figs. 9 and 10. The experimental results confirm that a phase shift between the carriers reduces the current ripple of i_{S3} but it negatively affects the torque ripple, which is proportional to the product $i_{Sd}i_{Sq}$. Moreover, i_{ch} affects the saturation level of the machine and the current ripple charts.

To further support the results of the theoretical analysis, the torque ripple generated by the machine was measured experimentally. Due to the 1 kHz bandwidth limitation of the torque meter (Kistler 4503A50) installed on the test bench, the switching frequency of the converter was reduced to 600 Hz to measure at least the first harmonic of the torque ripple waveform. The tests shown in Figs. 19 and 20 were performed

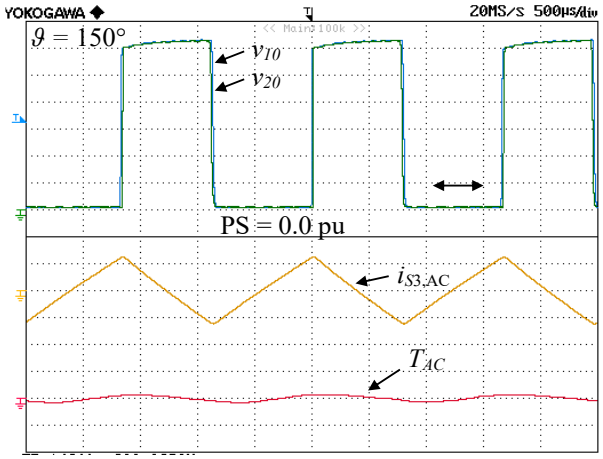

Fig. 19. Comparison of the current ripple $i_{S3,AC}$ and torque ripple T_{AC} when the phase shift is 0.0 pu. Waveforms of v_{10} and v_{20} (10 V/div), $i_{S3,AC}$ (1 A/div), and the AC component of the torque T_{AC} (100 mNm/div).

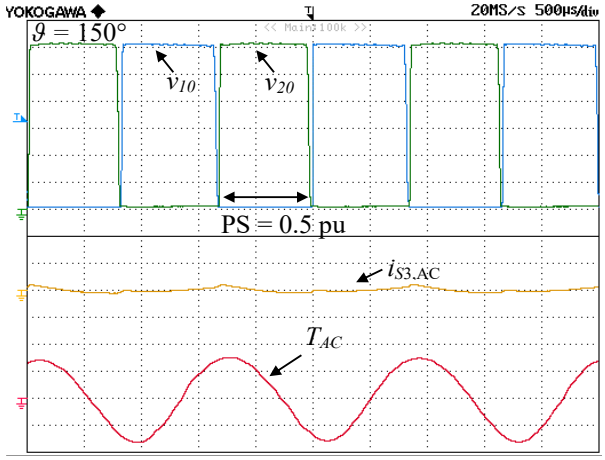

Fig. 20. Comparison of the current ripple $i_{S3,AC}$ and torque ripple T_{AC} when the phase shift is 0.5 pu. Waveforms of v_{10} and v_{20} (10 V/div), $i_{S3,AC}$ (1 A/div), and the AC component of the torque T_{AC} (100 mNm/div).

This work is licensed under a Creative Commons Attribution-NonCommercial-NoDerivatives 4.0 License.
For more information, see https://creativecommons.org/licenses/by-nc-nd/4.0/

This article has been accepted for publication in IEEE Transactions on Power Electronics. This is the author's version which has not been fully edited and content may change prior to final publication. Citation information: DOI 10.1109/TPEL.2026.3724067

with an i_{ch} = 15 A, at the angular position $\vartheta = 150°$, and with a phase shift of 0.0 pu and 0.5 pu respectively. The figures show the inverter pole voltages v_{10} and v_{20}, the current ripple $i_{S3,AC}$, and the AC component T_{AC} of the torque. The results confirm that a phase shift between the carriers reduces $i_{S3,AC}$ at the expense of an increased torque ripple. The tests of Figs. 19 and 20 were carried out at 600 Hz only to make the torque ripple observable with the available torque-meter bandwidth. Therefore, the measured torque ripple amplitude should not be considered representative of the nominal 10 kHz operation. For the same operating point and modulation index, the current ripple scales approximately with $1/f_{sw}$, and the dominant torque ripple component follows the same trend. Consequently, the 600 Hz measurements are used to validate the dependence of the torque ripple on the carrier phase shift, while the expected amplitude at 10 kHz is significantly lower and can be estimated through the analytical ripple model.

In conclusion, the choice of the PS is a trade-off between the maximum current ripple allowed by the off-board charger, the sizing of the decoupling capacitor C_{in}, the saturation level of the machine, and the vibration induced by torque ripple.

VI. Conclusion

This paper presents a method for adapting a high-voltage battery to the voltage level of an off-board charger by reconfiguring an electrical machine and a three-phase inverter into a DC/DC boost converter. The presented control scheme aims to regulate the charging current while maintaining a zero average shaft torque, regardless of the angular position of the rotor. Additionally, the current and torque ripple have been investigated as functions of the PS between the PWM carriers and of the magnetic saturation level of the machine. The theoretical analysis is consistent with the result obtained on a scaled-down test setup based on a SynRM. Although the experimental validation was carried out on a scaled-down test bench, the results confirm the proposed control principle and the predicted trade-off between charger-side current ripple and torque ripple. In a full-power vehicle implementation, additional aspects must be considered, including the higher semiconductor dv/dt, differential- and common-mode EMI, insulation stress of the machine windings, thermal management of the machine operated as a stationary coupled inductor, the RMS-current rating of the input capacitor, and the coordination of contactors and protection devices. These aspects do not alter the proposed control concept, but they must be addressed in the design of an automotive-grade system.

References

[1] F. J. Márquez-Fernández, J. Bischoff, G. Domingues-Olavarría and M. Alaküla, "Assessment of future EV charging infrastructure scenarios for long-distance transport in Sweden," *IEEE Trans. Transp. Electrif.*, vol. 8, no. 1, pp. 615-626, March 2022, doi: 10.1109/TTE.2021.3065144.

[2] B. Al-Hanahi, I. Ahmad, D. Habibi and M. A. S. Masoum, "Charging infrastructure for commercial electric vehicles: challenges and future works," *IEEE Access*, vol. 9, pp. 121476-121492, 2021, doi: 10.1109/ACCESS.2021.3108817.

[3] M. A. H. Rafi and J. Bauman, "A comprehensive review of DC fast-charging stations with energy storage: architectures, power converters, and analysis," *IEEE Trans. Transp. Electrif.*, vol. 7, no. 2, pp. 345-368, June 2021, doi: 10.1109/TTE.2020.3015743.

[4] H. Tu, H. Feng, S. Srdic and S. Lukic, "Extreme fast charging of electric vehicles: a technology overview," *IEEE Trans. Transp. Electrif.*, vol. 5, no. 4, pp. 861-878, Dec. 2019, doi: 10.1109/TTE.2019.2958709.

[5] P. Franzese *et al*., "Fast DC charging infrastructures for electric vehicles: overview of technologies, standards, and challenges," *IEEE Trans. Transp. Electrif.*, vol. 9, no. 3, pp. 3780-3800, Sept. 2023, doi: 10.1109/TTE.2023.3239224.

[6] C. Jung, "Power up with 800-V Systems: the benefits of upgrading voltage power for battery-electric passenger vehicles," *IEEE Electrif. Mag.*, vol. 5, no. 1, pp. 53-58, March 2017, doi: 10.1109/MELE.2016.2644560.

[7] A. Khaligh and M. D'Antonio, "Global trends in high-power on-board chargers for electric vehicles," *IEEE Trans. Veh. Technol.*, vol. 68, no. 4, pp. 3306-3324, April 2019, doi: 10.1109/TVT.2019.2897050.

[8] I. Aghabali, J. Bauman, P. J. Kollmeyer, Y. Wang, B. Bilgin and A. Emadi, "800-V electric vehicle powertrains: review and analysis of benefits, challenges, and future trends," *IEEE Trans. Transp. Electrif.*, vol. 7, no. 3, pp. 927-948, Sept. 2021, doi: 10.1109/TTE.2020.3044938.

[9] H. Muhedinovic, "DC charging compatibility - grappling with challenges between 800 V and 400 V", SAE World Congress Experience, Detroit, Michigan, April 5-7, 2022.

[10] S. Haghbin, S. Lundmark, M. Alakula and O. Carlson, "Grid-connected integrated battery chargers in vehicle applications: review and new solution," *IEEE Trans. Ind. Electron.*, vol. 60, no. 2, pp. 459-473, Feb. 2013, doi: 10.1109/TIE.2012.2187414.

[11] M. H. Kim, Y. S. Lim, S. C. Shin, K. H. Jeong, Hyundai Motor Co., Kia Co., *Electrified vehicle and method of controlling same,* U.S. Patent No. 20240039448A1 (2022).

[12] R. Raj, D. Singh, S. Halder, M. Diana, B. S. Ram and Y. Thioliere, "Finite Element Analysis of an IPM Machine for Charging Operations in Electric Vehicles," 2024 International Conference on Electrical Machines (ICEM), Torino, Italy, 2024, pp. 1-6, doi: 10.1109/ICEM60801.2024.10700232.

[13] M. Shao, Q. Zhang, Z. Wei and H. Guang, "Zero torque integrated on-board EV battery charger with enhanced winding filter inductance," *IEEE Trans. Power Electron.*, vol. 39, no. 8, pp. 9982-9995, Aug. 2024, doi: 10.1109/TPEL.2024.3400837.

[14] Y. Xiao and C. Liu, "A Study of Rotational Movement and Charging Torque of Reconfigured On-Board Charger," *IEEE Trans. Power Electron.*, vol. 35, no. 10, pp. 10720-10728, Oct. 2020, doi: 10.1109/TPEL.2020.2979349.

[15] M. Y. Metwly, M. S. Abdel-Majeed, A. S. Abdel-Khalik, R. A. Hamdy, M. S. Hamad and S. Ahmed, "A review of integrated on-board ev battery chargers: advanced topologies, recent developments and optimal selection of fscw slot/pole combination," *IEEE Access*, vol. 8, pp. 85216-85242, 2020, doi: 10.1109/ACCESS.2020.2992741.

[16] D. G. Woo, D. M. Joo and B. K. Lee, "On the feasibility of integrated battery charger utilizing traction motor and inverter in plug-in hybrid electric vehicles," *IEEE Trans. Power Electron.*, vol. 30, no. 12, pp. 7270-7281, Dec. 2015, doi: 10.1109/TPEL.2015.2396200.

[17] G. Pellegrino, E. Armando and P. Guglielmi, "An integral battery charger with power factor correction for electric scooter," *IEEE Trans. Power Electron.*, vol. 25, no. 3, pp. 751-759, March 2010, doi: 10.1109/TPEL.2009.2033187.

[18] S. Semsar, T. Soong and P. W. Lehn, "On-board single-phase integrated electric vehicle charger with V2G functionality," *IEEE Trans. Power Electron.*, vol. 35, no. 11, pp. 12072-12084, Nov. 2020, doi: 10.1109/TPEL.2020.2982326.

[19] H. J. Raherimihaja, Q. Zhang, T. Na, M. Shao and J. Wang, "A three-phase integrated battery charger for EVs based on six-phase open-end winding machine," *IEEE Trans. Power Electron.*, vol. 35, no. 11, pp. 12122-12132, Nov. 2020, doi: 10.1109/TPEL.2020.2986798.

[20] I. Subotic, N. Bodo and E. Levi, "Single-phase on-board integrated battery chargers for evs based on multiphase machines," *IEEE Trans. Power Electron.*, vol. 31, no. 9, pp. 6511-6523, Sept. 2016, doi: 10.1109/TPEL.2015.2504400.

[21] C. Shi, Y. Tang and A. Khaligh, "A Single-phase integrated onboard battery charger using propulsion system for plug-in electric vehicles," *IEEE Trans. Veh. Technol.*, vol. 66, no. 12, pp. 10899-10910, Dec. 2017, doi: 10.1109/TVT.2017.2729345.

[22] P. Pescetto, M. F. T. Cruz, F. Stella and G. Pellegrino, "Galvanically Isolated On-Board Charger Fully Integrated With 6-Phase Traction Motor Drives," *IEEE Access*, vol. 11, pp. 26059-26069, 2023, doi: 10.1109/ACCESS.2023.3256266.

[23] C. Viana and P. W. Lehn, "A drivetrain integrated dc fast charger with buck and boost functionality and simultaneous drive/charge capability," *IEEE Trans. Transp. Electrif.*, vol. 5, no. 4, pp. 903-911, Dec. 2019, doi:

This work is licensed under a Creative Commons Attribution-NonCommercial-NoDerivatives 4.0 License.
For more information, see https://creativecommons.org/licenses/by-nc-nd/4.0/

This article has been accepted for publication in IEEE Transactions on Power Electronics. This is the author's version which has not been fully edited and content may change prior to final publication. Citation information: DOI 10.1109/TPEL.2026.3724067

10.1109/TTE.2019.2925211.

[24] J. Yang, G. C. Lim, C. Hwang and J. -I. Ha, "Two-Phase DC Charging Method for Improved Efficiency and Zero Torque in Motor-Integrated Charger," *IEEE Trans. Ind. Electron.*, vol. 72, no. 5, pp. 4535-4545, May 2025, doi: 10.1109/TIE.2024.3468

This work is licensed under a Creative Commons Attribution-NonCommercial-NoDerivatives 4.0 License.
For more information, see https://creativecommons.org/licenses/by-nc-nd/4.0/